

Dipolar emission in trench metal–insulator–metal waveguides for short-scale plasmonic communications: numerical optimization

This content has been downloaded from IOPscience. Please scroll down to see the full text.

2014 J. Opt. 16 114006

(<http://iopscience.iop.org/2040-8986/16/11/114006>)

View [the table of contents for this issue](#), or go to the [journal homepage](#) for more

Download details:

IP Address: 137.73.5.232

This content was downloaded on 05/11/2014 at 18:59

Please note that [terms and conditions apply](#).

Invited Article

Dipolar emission in trench metal–insulator–metal waveguides for short-scale plasmonic communications: numerical optimization

Ryan McCarron¹, Wayne Dickson, Alexey V Krasavin, Gregory A Wurtz and Anatoly V Zayats

Department of Physics, King's College London, Strand, London, WC2R 2LS, UK

E-mail: r.mccarron@qub.ac.uk

Received 20 June 2014, revised 21 July 2014

Accepted for publication 21 July 2014

Published 3 November 2014

Abstract

Here we consider the numerical optimization of active surface plasmon polariton (SPP) trench waveguides suited for integration with luminescent polymers for use as highly localized SPP source devices in short-scale communication integrated circuits. The numerical analysis of the SPP modes within trench waveguide systems provides detailed information on the mode field components, effective indices, propagation lengths and mode areas. Such trench waveguide systems offer extremely high confinement with propagation on length scales appropriate to local interconnects, along with high efficiency coupling of dipolar emitters to waveguided plasmonic modes which can be close to 80%. The large Purcell factor exhibited in these structures will further lead to faster modulation capabilities along with an increased quantum yield beneficial for the proposed plasmon-emitting diode, a plasmonic analog of the light-emitting diode. The confinement of studied guided modes is on the order of 50 nm and the delay over the shorter 5 μm length scales will be on the order of 0.1 ps for the slowest propagating modes of the system, and significantly less for the faster modes.

Keywords: surface plasmon polaritons, surface plasmon waveguides, surface plasmon source, electroluminescent polymer

(Some figures may appear in colour only in the online journal)

1. Introduction

The drive towards decreasing dimensions of on-chip local and intermediate interconnects present many obstacles to the continued use of purely electronic communications; in particular increased RC delay in nanoscale interconnects [1]. These problems may be circumvented by nano-optical communications, which offer high confinement along with improved

communication speeds [2]. This paper investigates the viability of nanoscale electrically-driven luminescent devices for use in direct generation of surface plasmon polariton (SPP) mediated optical communications at the nanoscale.

Plasmonic waveguiding has been achieved in many forms, including slab waveguides [3], wire waveguides [4], dielectric or semiconductor-loaded waveguides [5, 6], and multilayer waveguides including insulator–metal–insulator (IMI) and metal–insulator–metal (MIM) geometries [7, 8]. These waveguides may be integrated with more complex media to provide

¹ Current address: Department of Physics, Queen's University Belfast, BT7 1NN, UK.

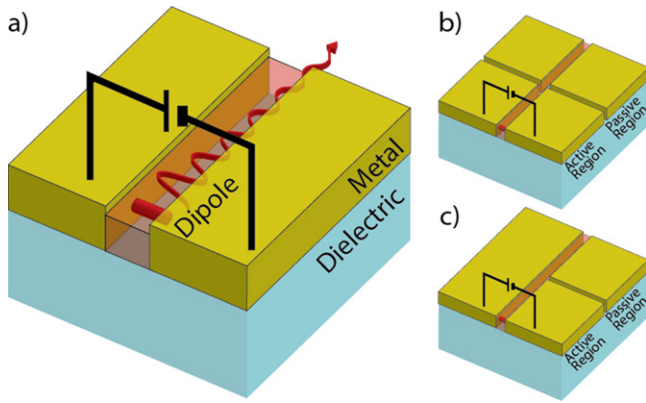


Figure 1. (a) Schematic of trench source system—the trench is filled with red-emissive electroluminescent co-polymer suited for plasmonic systems. (b) and (c) show possible geometries for ‘realistic’ SPP waveguide sources, with active emissive regions and passive guiding-only regions separated by either a double break or single break in the guiding trench wall, respectively.

features such as signal modulation, achievable through meta-material optical response [9], nanoscale electro-optical response [10], and auto-modulating systems [11]. Various waveguide structures have also been employed with conventional nonlinear media [12, 13], for the development of structures exhibiting net plasmonic gain [14, 15] within the limits of such strongly attenuating systems [16]. MIM SPP waveguides in particular have been extended to narrow MIM strips, to form ‘slot’ or ‘trench’ waveguides [17] (figure 1), which have recently been shown to exhibit suitability for integration with electrically driven emissive devices [18].

The necessity for an emissive material in an active, integratable plasmonic source device may be satisfied through any luminescent medium compatible with the chosen device geometry. Luminescent polymers offer several advantages over inorganic emitters when considering their application to a plasmonic device. In particular, the advantages of lessened refractive index with smaller impact on the SPP propagation length and greatly reduced necessity for processing in device fabrication opens up interesting applications for light sources for both the near field and far-field [19]. The ability to easily deposit organic material allows the development of devices with complex morphologies, including active plasmonic elements [20, 21]. Combining this material with plasmonic waveguide systems, one can make use of direct emission coupling to SPP modes; a loss channel in conventional OLED technologies [22] is here used for plasmon-emitting devices [23].

The role of a tightly confined plasmonic source can be played by a waveguide element filled with luminescent material. In a typical trench MIM waveguide system, the central guiding trench element can be filled with electroluminescent material, and the walls of this trench can act as both electrodes for emission excitation and as plasmonic waveguiding elements (figure 1). An MIM SPP waveguide structure necessitates symmetric metal layers, which will adequately support SPP modes while providing high confinement; however the asymmetric nature of such structures fabricated on a substrate of

some different refractive index to the luminescent medium provides a complexity to the modes extant in the system.

In this paper, we numerically investigate the optical properties of plasmonic trench waveguides with a view to their suitability for integration with electroluminescent copolymer. Photonic properties of suitable waveguides have been studied and waveguiding properties were optimized for pairing of an incoherent electrically pumped active waveguide ‘source’ driven by the spontaneous emission of a plasmon-emitting diode (PED—analogous to a LED) which is coupled to a passive waveguide element of the same dimension. An analysis of the coupling of an emissive dipole within the system to the various modes extant in the system, with optimization for plasmonic coupling, was then carried out.

2. Device structure

For all structures under investigation, we have chosen waveguiding components based on Au. The conjugated polymer emitter for this investigation was chosen to be compatible with the operating wavelengths of Au waveguides, and so was chosen to be poly(3-octylthiophene)-2,5-diyl (P3OT). P3OT has a band-gap of 1.72 eV and highest occupied molecular orbital (HOMO) energy level of -5.25 eV with respect to the vacuum level [24], and gives photoluminescence and electroluminescence with peak emission at 670 nm, making it well-suited for hybridization with Au waveguides. P3OT has been found to pack closely with spacings under 2 nm [25], making it well-suited for integration into narrow MIM structures.

The simulation of this waveguide was performed with Au (permittivity data from Palik [26]) on a glass substrate of refractive index 1.5, and filled with polymer P3OT which is assumed for this model to be deposited at sufficient thickness to allow no further superstrate layer to modify the properties of modes existing within the trench. The refractive index data for this polymer was obtained from studies on the anisotropy of thin P3OT films [27].

3. Waveguide optimization

We have used finite element method software (COMSOL Multiphysics) to analyze the waveguide elements and optimize these guides towards forming an effective electro-optical transducer. The geometry of the waveguide was optimized with respect to the waveguiding properties of mode area and propagation length, which uses a figure of merit (FoM) [28]:

$$M = \sqrt{\frac{\pi}{A_{\text{eff}}}} \frac{1}{\text{Im}(k_{\text{spp}})}, \quad (1)$$

where A_{eff} is the effective SPP mode area and k_{spp} is the surface plasmon wavevector.

3.1. Eigenmode analysis of ideal structures

Eigenmode analysis was performed for the waveguides in figure 2, assuming infinite waveguide length, width specified

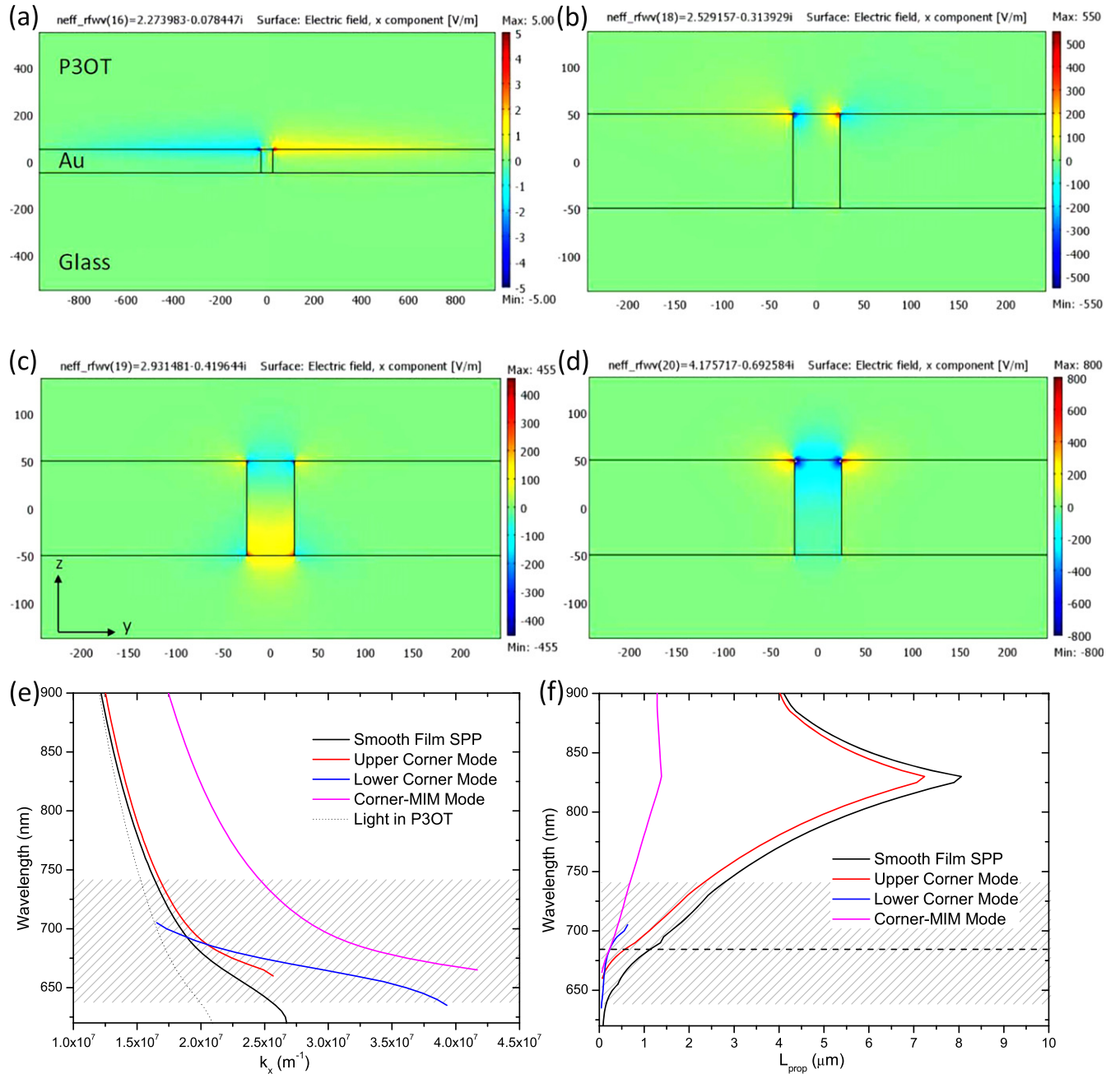


Figure 2. E_x mode profiles at $\lambda_0 = 670$ nm and dispersion of surface plasmon modes in a 50 nm wide trench in 100 nm Au on glass with P3OT superstrate and trench medium. (a) Shows the smooth film mode, supported in part by the PEC walls of the model, with some small component of the mode existing in the central trench. (b) Shows the mode supported by the corners of the trench and extending partially into the superstrate. (c) Lower trench corner mode, which exhibits a cut-off for $\lambda_0 > 710$ nm, which exhibits much greater confinement in comparison to the mode in (b). (d) Fundamental trench mode, which exhibits high confinement (a)–(d) show the x -component of the electric field for the various modes. (e) Shows dispersion of the modes found in (a)–(d), showing cut-off of the lower corner mode. (f) Shows the imaginary part of the dispersion in the form of propagation length of each of these modes, maintaining the loss of propagation for highly confined modes. (e) and (f) display the full width half-maximum (FWHM) emission of P3OT in the grey hashed area, with peak emission at $\lambda_0 = 670$ nm marked by the horizontal dashed line.

by the central guiding element filled with polymer, and height determined by Au film thickness.

Eigenmode simulation determined a number of modes within the system. Excluding photonic modes existing in the media adjacent to the structure and modes which can leak into the substrate, the waveguiding modes can be classified into five distinct categories (figure 2): smooth film modes on the superstrate or substrate interface, corner modes localized at

the sharp vertices of the trench and the superstrate or the substrate, and fully ‘bound’ trench modes existing only in the narrowest trenches (i.e. 20 nm width and below). The SPP modes at the P3OT–Au interface exhibit low confinement and are included for reference. No photonic modes were observed within the trench waveguide, drastically reducing the photonic loss channels available to radiating dipoles within the trench.

The dispersion of the mode supported by the upper corners of the waveguide behaves as a slight modification to the smooth film SPP; this is expected from the mode profile, as a considerable fraction of the mode is located on the smooth film interface. This mode has some extension to perfect electric conductor boundary conditions, which enable this mode (the only mode with significant boundary interaction) not to suffer attenuation by the model walls which would be the case for any scattering boundary conditions. This mode is antisymmetric in E_x . A lower-corner mode (figure 2(c)) is symmetric in E_x and retains localization of the electric field to both the upper and lower interfaces, and exhibits greatest localization near the substrate boundary. This mode also exhibits a node in E_x between the substrate and superstrate interfaces, and further exhibits a distinct cut-off as it approaches the maximum wavevector for light in P3OT. Below this threshold, a mode with similar field profile and localization exists; however it is unbound and exhibits significantly increased propagation and decreased confinement, making it unsuitable for waveguiding.

The mode exhibiting greatest effective index is a symmetric mode localized partly to the upper corner, which due to the significant field fraction within the bulk of the trench is termed a hybrid corner-MIM mode with symmetric E_x . This mode is approximately uniform across the trench, with a small localization to the superstrate corner due to the asymmetric nature of the system. This mode retains a significant field fraction within the waveguide, and so localization to the polymer layer makes it ideal for coupling dipoles existing within the trench in a plasmonic source device.

The propagation length (L_{prop}) of these high-confinement modes is extremely short. For $\lambda_0 = 720$ nm, L_{prop} for the highly confined modes is on the order of $1 \mu\text{m}$ (figure 2(f)) which can be useful for short communication scales. Increasing the wavelength moves beyond the cut-off of the lower-corner mode, leaving the corner-MIM mode as the remaining high-confinement mode.

The mode properties will also exhibit significant variation with trench width and thickness. Due to the increased confinement offered for decreased widths, the system tends to the infinite MIM system. This can be clearly seen in figure 3, which shows decreasing trench width for all thicknesses significantly decreases propagation length and increases the effective index for the modes shown in figure 2. The increase in aspect ratio of the trenches allows the formation of true MIM TM (m, n) modes, where m and n represent the number of antinodes in the electric field intensity in x and y , respectively, similar to those seen in symmetric MIM systems. With increasing aspect ratio, plasmonic modes 'see' less of the dielectric outside the trench system, which gives a tendency towards these confined higher-order modes seen in the symmetric system.

While the majority of the trench-supported modes exhibit increased effective index and decreased L_{prop} for increased aspect ratio, the antisymmetric mode on the upper corners of the system instead tends to a less-confined, lower-loss mode extending into the superstrate. The central node reduces the field intensity within the trench, causing field extension into the surrounding polymer.

These modes exhibit many desirable properties for use as optical interconnects, including high confinement and a group velocity of between $0.05c$ and $0.26c$ (calculated from the mode dispersions) for the modes within the FWHM window of the P3OT emission (figure 4). The confinement of these modes was established by determination of the mode area acquired numerically from the eigenmode analyses. These values can be used to produce a FoM, as seen in equation (1) to depend on the imaginary component of the SPP wavevector (or interchangeably propagation length) and the mode area (figure 4(c)) calculated through integration of the electric field over the mode cross-section. The FoM clearly indicates the lower corner mode to be the most favourable for signal waveguiding purposes, particularly for lower trench widths, with the MIM (1, 1) mode providing a similar effectiveness for the narrowest waveguides. For wider trenches, the more confined upper corner and corner-MIM modes become comparable to the lower corner modes.

However, this FoM fails to take into account the group velocity v_g of the modes which is also correlated to the local density of photonic states, D , important for emission properties in these modes, which exhibits a dependency of $D(\omega)\alpha v_g^{-3}$ [29].

By including a term of v_g/c in FoM and applying this to the 100 nm Au trenches of 100 nm width, the lower corner mode clearly becomes the most heavily favoured. Further, the properties of the corner-MIM mode and the upper corner mode become more distinct due to the added factor of increased group velocity of the latter mode. For 100 nm width trenches shown in figure 4(b), the FoM for lower corner, upper corner and corner-MIM modes are 0.730, 0.131, and 0.081 respectively. This picture of the mode properties indicates that coupling to the lower-corner modes should be prioritized for application to real-world devices.

The mode areas observed further exhibit distinct oscillations in confinement with decreasing trench width and, thus, FoM, without any significant oscillation in propagation length or effective index. This behaviour is most likely due to the change in aspect ratio and effective index causing vertical Fabry–Pérot effects to modify the spatial extent of the mode for the least-confined regions, while the complex effective index remains relatively unmodified due to the areas of greatest field intensity remaining unaffected by this shift, i.e. the supporting corners. The oscillation effects are most strongly observed for the corner-MIM mode, which has a significant field fraction inside the trench, and thus becomes more susceptible to this Fabry–Pérot oscillation. The lower and upper corner modes, while exhibiting some variation, display less significant oscillation, most likely due to lack of confinement to the trench and field extension primarily into the substrate.

3.2. Eigenmode analysis of realistic structures

The structures analyzed so far have been highly idealized; the trench walls are entirely perpendicular to the film and the edges are perfectly sharp at 90° . A more realistic case would be the rounding of these corners by some radius of curvature r_c . For realistic systems made with focused ion beam (FIB)

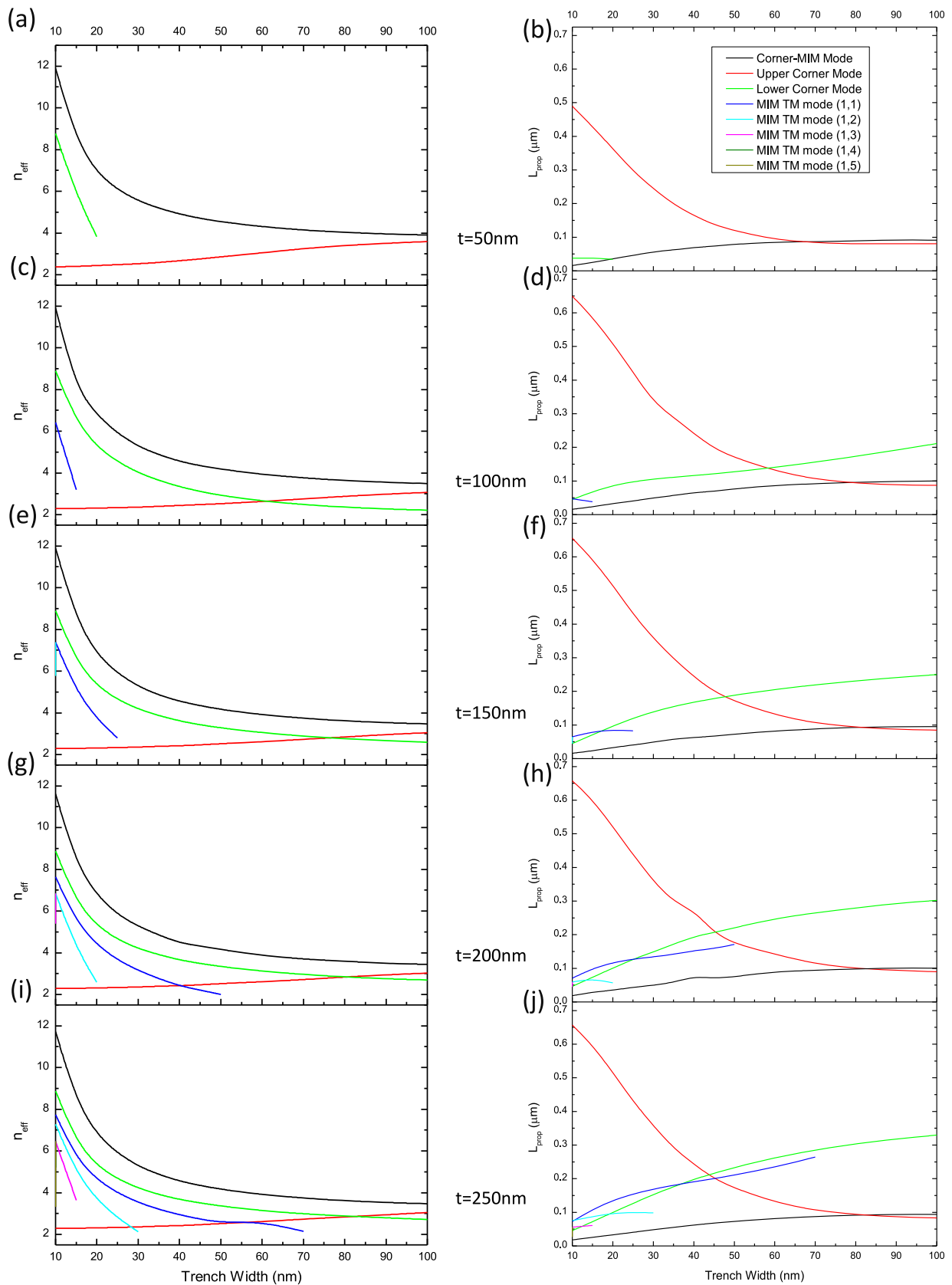


Figure 3. Variation of mode properties within the trench with varying trench width and thickness, t at $\lambda = 670$ nm. (a), (c), (e), (g), (i) show the effective indices of the trench modes for Au thicknesses 50–250 nm, and width 10–100 nm. (b), (d), (f), (h), (j) show the propagation lengths of the same modes over the same structural ranges. Figures clearly indicate the cut-off of fully MIM modes, as well as decreasing propagation length for decreasing trench width for all modes except the lower corner mode, which gradually evolves into the surrounding dielectric for decreasing trench width. The modes also display a general trend towards increasing propagation with increasing Au thickness.

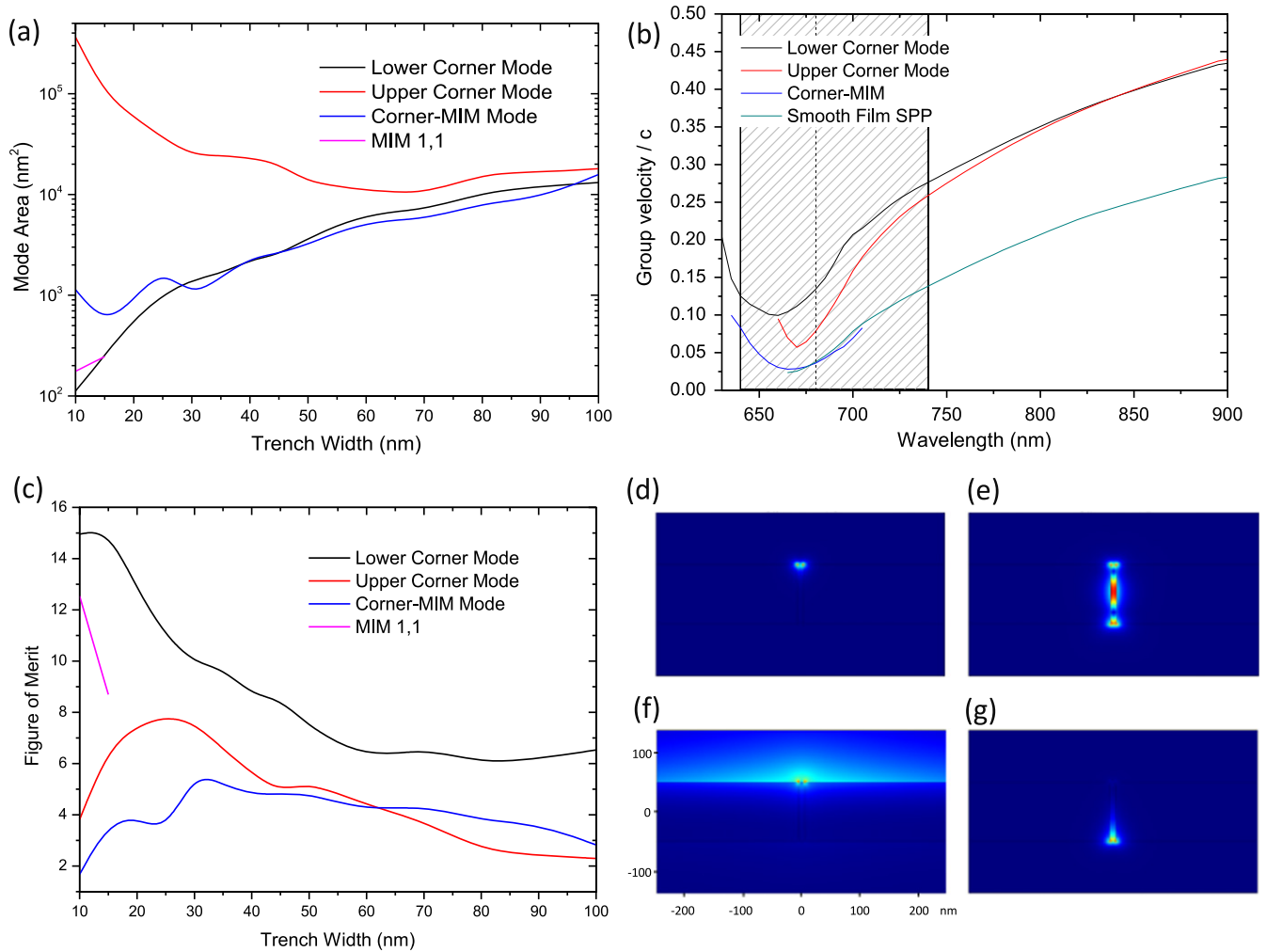


Figure 4. The mode properties and field profiles of 100 nm Au trench waveguides of varying width at $\lambda_0 = 670$ nm. (a) Shows varying modal areas of each of the modes shown previously with trench width, clearly displaying the evolution towards extremely low confinement in the upper corner mode. (b) Shows the group velocity of these modes for 100 nm width (seen in figure 2) as a fraction of c , which can determine their applicability to interconnects, with P3OT emissive region as shown previously. (c) Shows the variation in figure of merit for these waveguides over the variation shown in (a). (d)–(g) show mode profiles of the corner MIM, MIM (1, 1), upper corner and lower corner modes respectively in $|E|$ for 10 nm trenches.

milling, this can be taken as 10 nm. For structures manufactured with lift-off electron beam lithography (EBL) and treated with both O_2 plasma and Ar^+ milling, there will likely be a small rounding at the lower interface due to some shadowing of the Au deposition by the resist, which is again taken as 10 nm. This rounding can be expected intuitively to strongly modify the modes supported by the sharp Au corners.

As seen in figure 5, the corner modes remain in existence within the system despite this significant deformation, albeit strongly modified. The corner-MIM mode now exhibits an effective index approximately half that of the ideal system for narrow guide widths. However, this leads to an increase in propagation length by a factor of about 4 for 10 nm guides, and 2.4 for 50 nm guides. The rounding also provides a reduction in mode area for the 10 nm guides, by a factor of 0.49, with a slight increase by a factor of 1.2 for 50 nm guides. This leads to a net increase in FoM for this mode to

become comparable that of the lower corner mode in the idealized system for narrow guides, and overall improved for guides of 50 nm width.

The lower corner mode in this rounded system displays a cut-off at 70 nm, along with vastly reduced propagation length, and thus FoM, indicating this mode to be entirely unsuitable for waveguiding. This greater sensitivity to the geometry indicates this mode can be considered a loss channel for ‘real’ structures; however this may be rectified in fabrication through use of appropriate techniques.

All modes of this system exhibit oscillations with trench width as seen previously for idealized waveguides. In particular, examination of the lower corner mode reveals oscillations in both mode area and L_{prop} with trench width similar to those seen in the FoM in figure 4(c), posited to be related to Fabry–Pérot oscillations. This indicates a stronger modification of the field within the trench due to lowered confinement at the corners, seen in figure 5(g).

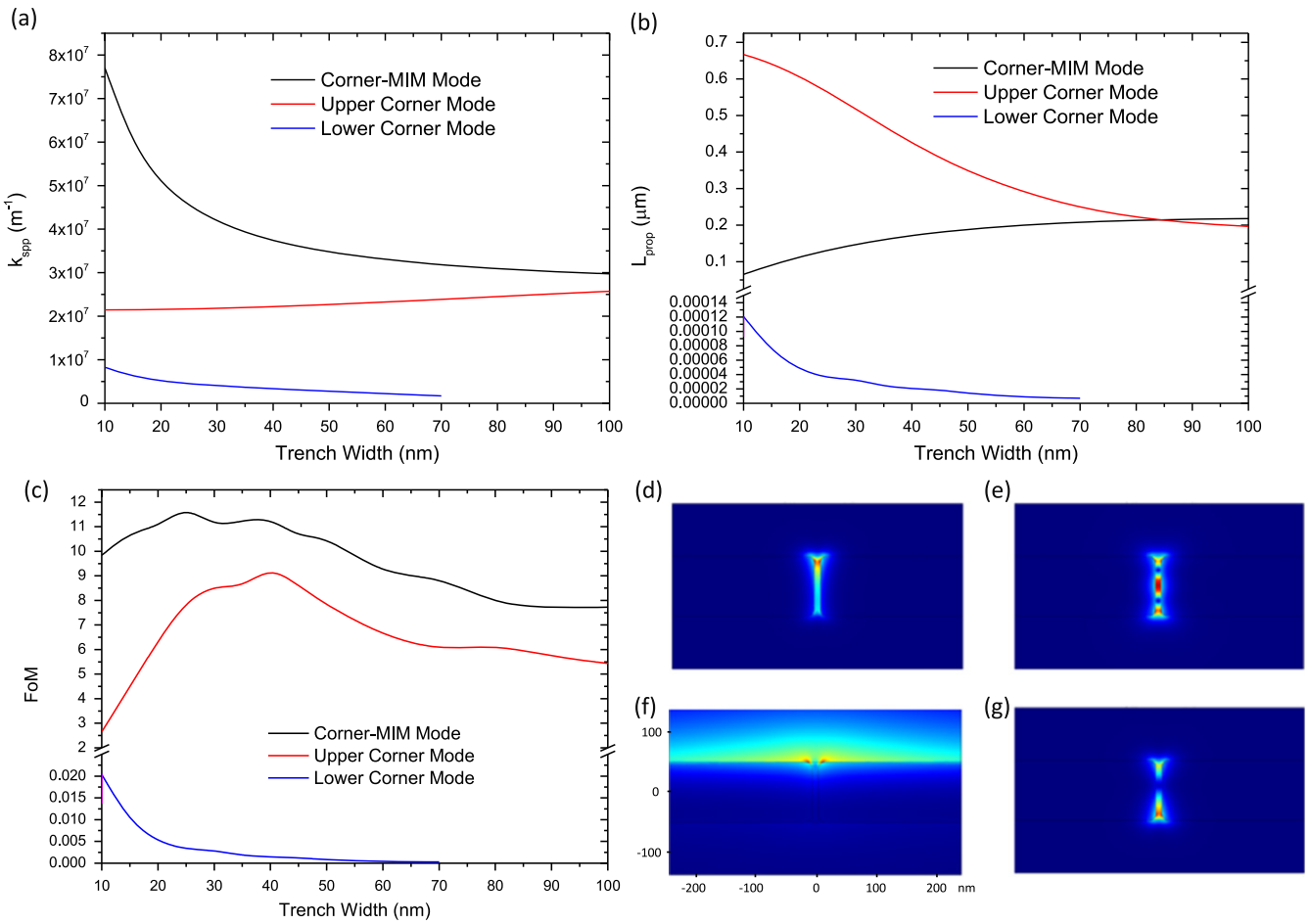


Figure 5. The mode properties of 100 nm Au trenches with rounding $r_c = 10$ nm at $\lambda = 670$ nm for varying trench width. (a) Shows the variation in k_{spp} at for the modes shown previously in the ideal system, with a cut-off for the lower corner mode at $w \approx 70$ nm. (b) Shows variation in propagation length for these same modes. (c) Shows variation in figure of merit for these modes with mode areas calculated as before. (d)–(g) show the various mode profiles in $|E|^2$ for these modes, with the same layout as figure 4. These profiles are for trench width 10 nm.

Decreased confinement is further exhibited by the remaining modes, i.e. the upper corner and MIM (1, 1) modes. For the upper corner mode, this is balanced by an increase in propagation length for 50 nm waveguides, allowing the FoM to remain of similar values to the ideal case. The MIM (1, 1) mode exhibits a decreased cut-off to 10 nm, which along with extremely short propagation length, leaves it unsuited for practical waveguiding use.

For 100 nm thick trench waveguides, the ideal structure with perfectly sharp edges indicates an ideal guide width of 10–20 nm, with emission preferentially coupling to both the upper corner mode and lower corner modes. However examination of the realistic case of small curvature at the upper and lower vertices indicates an optimum dimension for fabricated guides of 40–50 nm width. Although variation in thickness allows propagation of higher order MIM modes, to avoid multi-mode interference and maximize coupling efficiency into as few modes as possible, 100 nm Au thickness can be said to be optimum for waveguiding.

3.3. PED and waveguide integration

The structures to be created will necessarily consist of two distinct waveguiding regions for a useful plasmonic system—an electrically active region, and a separate, electrically isolated guiding region (figures 1(b) and (c)). For the structure given, the simplest and most effective mechanism for electrical isolation will be a break in the guide, either through either each wall (a double break) or a single wall (single break), as shown in figures 6(b) and (c). This was investigated using a 100 nm width MIM waveguide in 2D with Au walls and filled with P3OT. While this restricts analysis to the symmetric MIM mode, it can nevertheless produce a clear picture of the effect of modifications to this geometry on the mode properties.

The model used to determine the effects of isolation segments used eigenmode analysis to determine the mode properties of this infinite MIM guide at $\lambda = 670$ nm, which were then passed to a 2D model of the same dimensions and allowed to propagate along the guide into which a break had

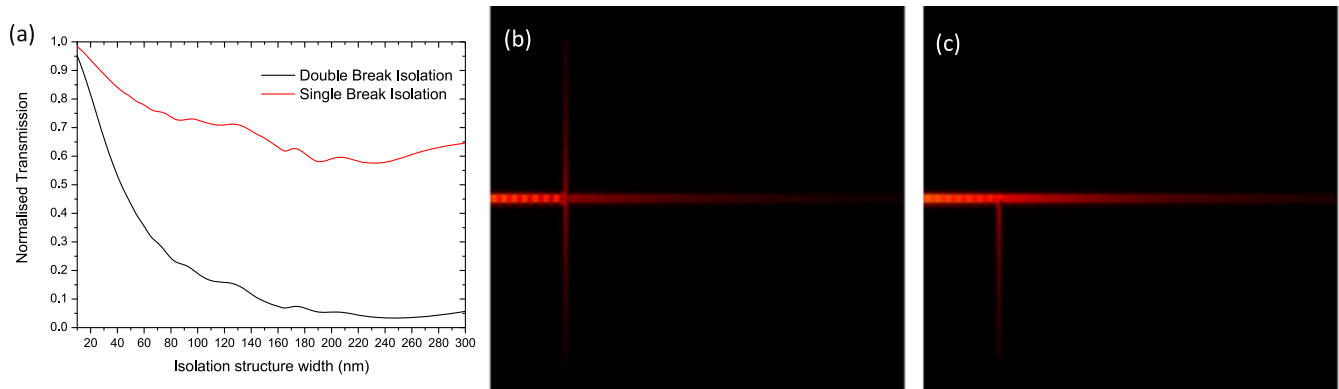


Figure 6. The transmission of an MIM waveguide at $\lambda = 670$ nm across electrical isolation segments. (a) Shows the transmission along an $8 \mu\text{m}$ guide for various isolation structure widths for both single-break and double-break isolation. (b) and (c) show field intensity leaking into the isolation trench for single-break and double-break isolation, respectively.

been introduced. While this system cannot replicate the complex mode structure of the 3D system, it provides valuable insight into plasmon tunnelling through a nanoscale gap while computationally less intense than the 3D system.

The ‘active’ guide region edge was taken as $1 \mu\text{m}$ from the model source, and a break of varying width filled with P3OT was introduced at this edge. The edge of this region marking the beginning of the break was fixed at $1 \mu\text{m}$ to avoid Fabry–Pérot oscillations in the active region with varying break width, and the remaining guide length and break width together make up $8 \mu\text{m}$ which terminates in a time-averaged power integration region (obtained through the Poynting vector at the surface) to define transmission and subsequent perfectly matched layer (PML) to remove reflection interference. PML regions were also defined within each electrical isolation region to act as loss channels for long isolation structures.

The isolation segment width was shown to significantly modify the transmission of the structure (figure 6(a)). Double-break isolation with the break trench width 150 nm will cause a reduction of up to 97% in transmission compared to the unmodified MIM guide. A single break performs much more effectively, with maximum reduction of 42%. This is due to the coupling of the surface plasmon across the trench—a narrow gap would require the surface plasmon to entirely tunnel across, however if one wall remains the plasmon can be partially supported through the gap, reducing the tunnelling barrier. As might be expected, a large isolation structure reduces the ability of the surface plasmon to couple across the gap into the remaining guide segment; for the narrowest separations of 10 – 20 nm, reduction in transmission is less than 5%. For feasibly fabricable structures of 50 nm, the reduction in transmission remains under 20% for a single break structure, indicating this to be a favourable outcoupling design.

3.4. Emitter-plasmon coupling in the waveguide

To achieve the best performance of the PED (driven by the spontaneous emission), we must find an optimization between waveguiding in the structure and the coupling of emitting dipoles to SPP modes, dependent strongly on the local density

of optical states. The analysis of dipole coupling to waveguide modes can be determined through finite simulations in both 2D and 3D. An emitting dipole, treated as a point and driven at the desired frequency is located in the central area of the trench, with an area of integration to observe transmission set some distance away, as seen in the schematics in figure 7. Selection of various emission wavelengths for the dipole allows useful determination of the spectral output of waveguides, while geometric variations allow observation of the effects of dipole orientation on surface plasmon coupling, and determination of a Purcell factor for the dipole inside the trench.

A finite 3D model was created of a trench waveguide on glass with 100 nm Au and 100 nm trench width. A dipole was located in the centre of the trench filled with P3OT, oriented normal to the trench walls, and an integration area was defined $4 \mu\text{m}$ from the trench centre, set to 150 nm in width and height and centred with respect to the waveguide, to measure modes both within the dielectric portion of the trench and extending to the metal and surrounding dielectrics. This detection region integrates the time averaged power flow and normalizes this to the total power input to the system, set at 1 W, to define transmission. The dipole was rotated to angles up to 90° with rotation axis both normal to and perpendicular to the trench walls, and a comparison made with the collection from the same area with the dipole emitting into free space (figure 7).

The dipole emission in free space behaves as expected, with the electric field oriented along the dipole axis, and rotation of the dipole parallel to the detection plane giving no change in transmission. The more interesting case of the dipole emitting inside the trench indicates transmission to the detection area to be strongly polarization dependent, and coupling to surface plasmon modes to be the dominant power transmission mechanism. As seen in figure 7(c), the decrease in transmission is not monotonic with increasing angle. This is due to the hybrid nature of the SPP modes—the dipole with some angle of rotation provides stronger field components in the required orientation, allowing more effective coupling. Additionally, the location of the dipole in the trench centre is unsuited to coupling to the modes existing primarily on the

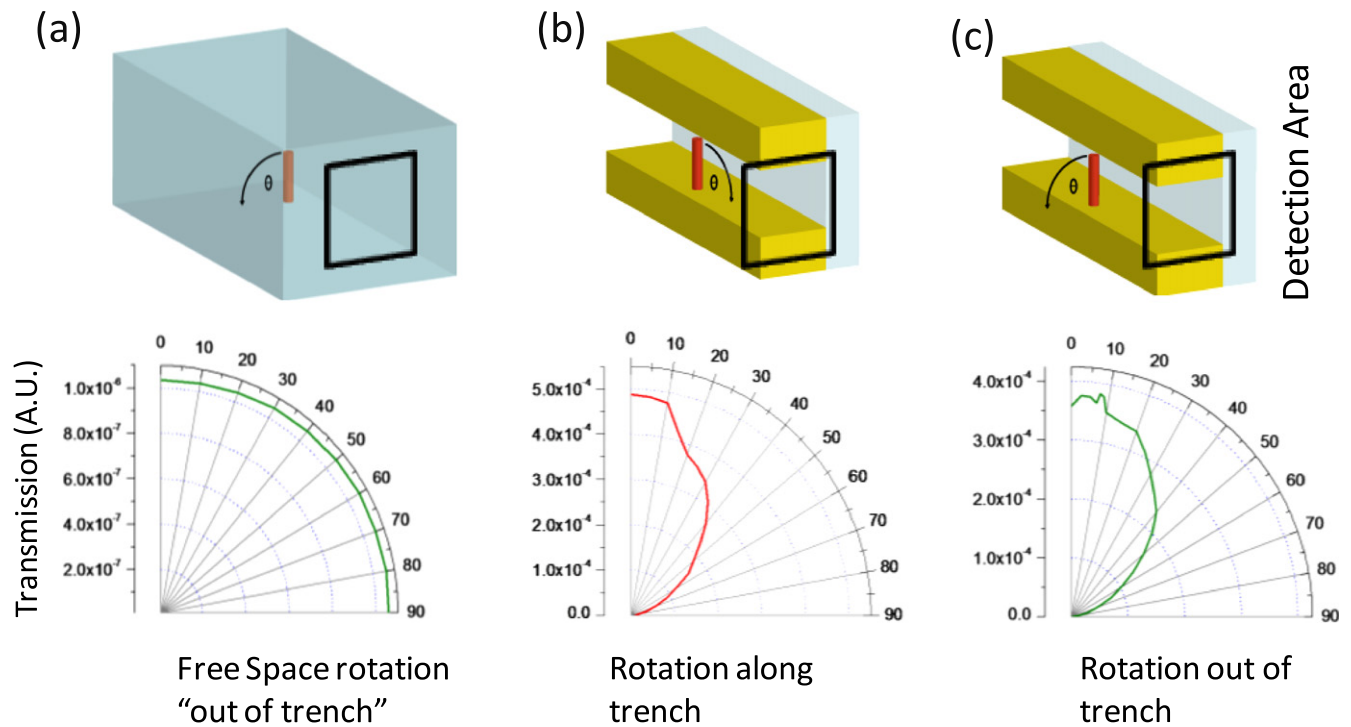


Figure 7. The effects of dipole rotation on emission through the trench waveguide. (a) Shows dipole rotation with rotation axis normal to the plane of detection. (b) Shows rotation of the dipole located in the centre of a 100 nm trench and decreasing transmission with increasing angle with rotation axis normal to the substrate plane. (c) Shows the same dipole with rotation axis normal to the plane of detection, and net decreasing transmission.

trench corners; an offset dipole or a dipole with slight rotation should allow greater coupling efficiency.

The dipole emitting in the trench centre will be subject to modifications of the electric field at the dipole due primarily to the SPP modes, and will see significant modifications to the radiative lifetime dependent on the dipole location within the trench due to significant variation in the dipole interaction with the various decay channels available [30]. We can consider these decay channels as both guided and non-guided radiative modes (both photonic and plasmonic modes) and non-radiative, such as quenching effects.

The Purcell factor [31] (F_p) of this dipole can be determined through the factor of increase in the total power radiated by the dipole at its position within the trench relative to emission in free space [32]. F_p was determined using the same configuration as the previous analysis for rotational analysis of the dipole. The dipole was located in an Au trench on a glass substrate filled with P3OT of 4 μm length. The power radiated by the dipole was determined through surface integration over a sphere encapsulating the point dipole with radius 1 nm. This same numerical analysis was performed on a dipole in P3OT, to determine F_p for the dipole radiating at various positions within the trench.

Figure 8 shows the Purcell factor for a dipole emitting at $\lambda = 670$ nm within the trench. The dipole location was varied up to 10 nm from the trench walls, beyond which quenching effects would be expected to dominate. The variation in F_p across the trench shows significant enhancement ($F_p = 28.7$ for a dipole normal to the walls) at the upper

corners, adjacent to the P3OT bulk, with enhancement at the substrate edge of $F_p = 23.9$. The variation in F_p indicates greatest enhancement due to coupling to surface plasmon modes. The eigenmodes of the system also determine a low local density of photonic states within the trench itself; photonic emission is inhibited and emission is driven towards SPP modes only.

The enhancement adjacent to the lower corner mode of the trench is seen to be lower than that for the upper corner and corner-MIM modes, which arises due to the field confinement of each of these modes into the trench; the lower corner mode has overall less confinement to the trench and the corners than both of the upper corner modes, which reduces SPP-dipole interaction.

This analysis was performed for the three orthogonal dipole orientations, with greatly reduced enhancement for the dipole parallel to the substrate, with a maximum F_p of 8.6 for the upper corners, and 1.3 in the trench centre. For the dipole parallel to the substrate, minor enhancement was observed close to the corners (with $F_p = 4.9$ for the upper corners) and inhibited emission was observed in the trench centre, with $F_p = 0.14$. The enhancement at the upper corners for these dipole orientations is due again to the hybrid nature of these modes and the range of field components in the near-field of the dipole. The inhibition in the centre is due to non-interaction with SPP modes existing in the system and the inability for the system to support photonic modes; the local density of states at the trench centre for this dipole can be said to be extremely low.

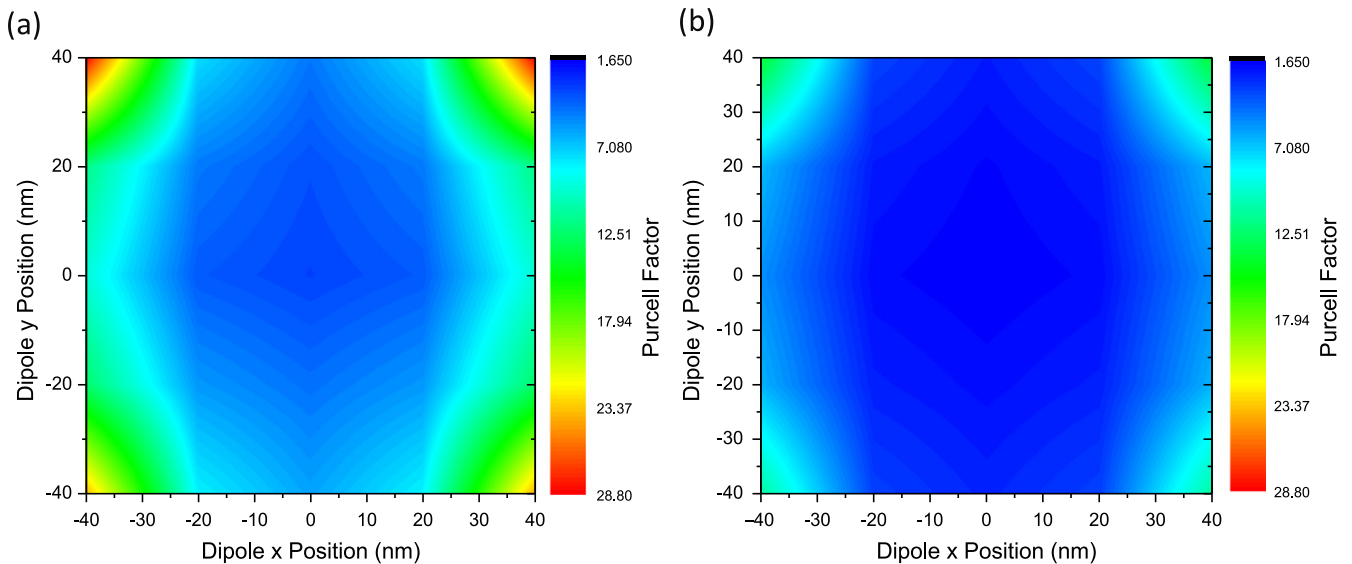


Figure 8. Purcell factor of a dipole located within a 100 nm Au square profile trench emitting at $\lambda = 670$ nm. (a) Shows the Purcell factor for varying x - and y -offsets within the trench for a dipole oriented normal to the trench walls. (b) Shows the Purcell factor experienced by an isotropic dipole emitting at each location.

The enhancement factor of each of these dipole orientations can be combined in average to determine the modification to an isotropic case, in which dipoles can be assumed to be randomly oriented. This maintains significant enhancement factors of $F_p = 14.1$ at the upper corners and $F_p = 11.1$ at the lower corners. While this gives an isotropic enhancement factor, the more strongly driven component of the dipole normal to the trench walls results in significantly lowered lifetime for dipoles of this orientation, is expected to result in preferentially polarized emission from the system due to relative suppression of the remaining dipole orientations.

The position of the dipole within the fields of the modes shown figure 2 will give a strong dependence on emission enhancement, and thus coupling to the system will depend strongly on the geometry of the waveguide.

The previous modelling was performed with the dipole located in the centre of the trench for orientations normal to the trench walls and normal to the substrate. The dipole was driven to emit at 670 nm, and the radiation allowed to propagate over $4 \mu\text{m}$ to the end of the trench, where a detection area was defined encompassing the waveguide core cross-section and an additional 25 nm on each side. This area is defined to collect primarily radiation only within the trench and localized to the corners.

Varying the width of the guide has been shown to strongly modify the extent of the fields inside the trench as well as their intensities—a narrower waveguide should exhibit more effective coupling to modes confined more strongly within the trench. This can simply be observed in the transmission of a section of waveguide containing a dipole source at various trench widths.

The variation in transmission for each dipole is shown in figure 9. For the dipole normal to the substrate, limited coupling to trench modes is expected, with some small coupling

to the corner modes available. The large transmission for wider trenches is due to coupling to the surface modes, which have some small component within the trench. The wider trenches allow the dipole to have a greater overlap with the field of these surface modes, while for narrower trenches, the field is localized almost entirely to the surface, reducing coupling and the portion of the surface mode existing within the detection range and thus transmission.

The dipole normal to the trench wall provides a view of preferential coupling to the surface plasmon modes. As trench width decreases, the propagation length of the modes existing within the system decrease, which should result in decreased transmission. However, figure 9(a) clearly shows a net increase in transmission for decreasing width, peaking for trenches of 20 nm width. This is due to the increased coupling available to the SPP modes for narrower trenches; from the Purcell enhancement seen in figure 8, the increased proximity to the trench walls indicates an increased power output from the dipole and enhanced coupling, which is sufficient to compensate for the increased losses and provide net transmission enhancement.

Figure 9(a) also shows a distorted increase in transmission for trench widths of 60 nm. This is due to the significantly increasing propagation length for the upper corner mode, which has not yet evolved out of the guide sufficiently to decrease coupling, which will provide additional enhancement of the emission into the guide. Below 20 nm there is the cut-on of the MIM (1, 1) waveguided mode, along with various additional waveguided modes of higher order and shorter propagation length, which will act partially as a loss channel, along with quenching for shortened dipole-metal separation.

The primary mechanism for energy transport to the detection area for emission in this case can be determined (for narrow guides) from the electric field profile of the system.

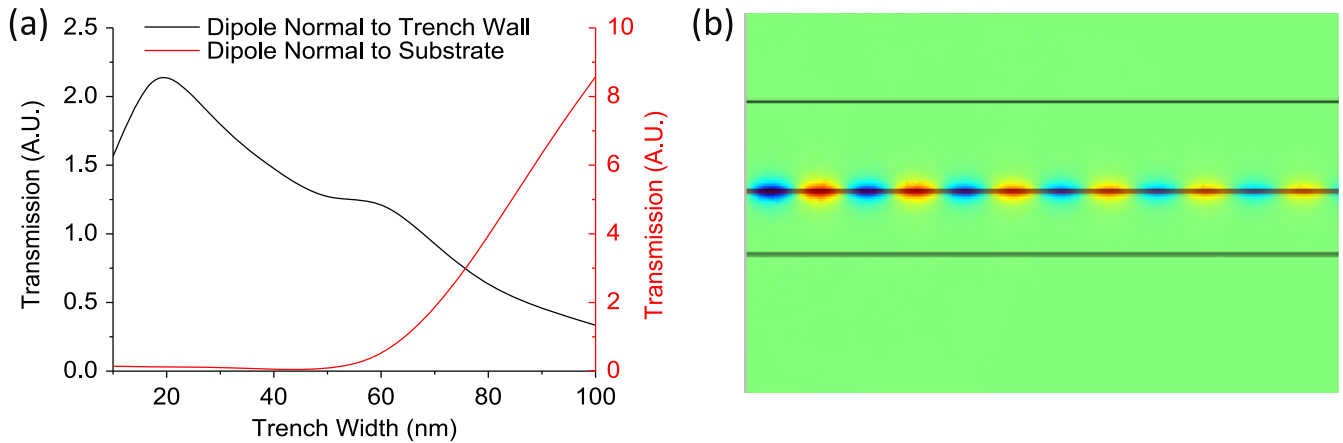


Figure 9. The dependence of trench transmission for 100 nm Au/P3OT trench on glass on trench width for two dipole orientations at 690 nm. (a) Shows the variation in transmission for dipoles normal to the trench wall and normal to the substrate for various widths. (b) Shows E_z for a dipole normal to the trench walls in a 10 nm trench.

Figure 9(b) shows the E_z profile for 20 nm trench, with effective index determined from the wavelength seen in this profile to be $n_{eff}=3.19$, matching that for the MIM (1, 1) waveguided mode for this system, indicating this mode dominates energy transport.

The result for Purcell factor shown in figure 10 cannot distinguish between radiative and non-radiative dipole enhancement. Further, while non-radiative decay in the form of coupling to surface plasmon waveguided modes must be enhanced, it is desirable to avoid non-radiative coupling to loss channels such as quenching. The coupling to surface plasmon modes can be determined through analysis of the decay in power flow along the trench, which should form an exponential function or a sum of exponential functions dependent on location and the number of concurrent modes propagating. This analysis was achieved through insertion of planes sampling the power flow at a separation of 50 nm throughout the length of the waveguide to determine the primary modes for transport and their coupling efficiency from the dipole, which was determined through extrapolation of a single exponential propagation to the dipole source and normalization to the total radiated power by the dipole within the trench, as seen in figure 10.

The coupling efficiency to the SPP modes shows a clear increase with decreasing trench width for all trench modes up to 60 nm, at which point coupling efficiency begins to decrease as losses to quenching become significant. The coupling fraction to the upper half of the system exhibits strong variation with position along the guide, due to oscillations in the mode location along the guide, most likely that of the corner-MIM mode which does not exhibit strong confinement to the corner. However, the overall fraction of the mode in the upper half of the system is seen to be larger than that of the lower half, indicating a preferential coupling to the upper corner and corner-MIM modes. This is due to the significant spatial overlap of these modes with the dipole allowing enhanced dipole–plasmon interaction and coupling. For extremely narrow trenches, the coupling fraction to the

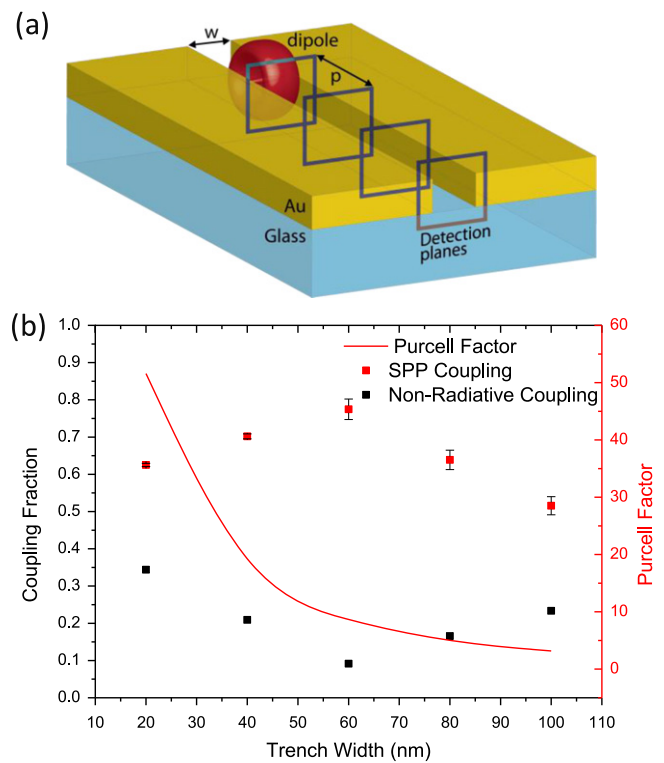


Figure 10. An analysis of coupling to plasmonic modes under varying trench width at $\lambda=670$ nm. (a) Shows the schematic analysis structure of 100 nm Au on glass filled with P3OT. Trench width w is varied from 20–100 nm with the dipole maintained at the central point of the trench. Integration is performed over detection planes at 50 nm separations to determine exponential SPP decay. (b) Shows the coupling fraction of total dipole radiated power to plasmonic modes, both in the upper half of the trench and the lower half. Uncertainty in the coupling is derived from fitting the plasmon exponential decay, which exhibits interference between co-propagating modes. Non-radiative coupling is shown as black squares. The Purcell factor for the dipole is shown as the red line plot.

upper half of the guide is diminished due to the cut-on of the MIM (1, 1) mode.

The Purcell factor for the dipole located in the trench centre and normal to the walls exhibits significant

enhancement for narrowing trench width as may be expected from the enhanced field confinement; this enhancement is sufficient to counteract the reduced coupling efficiency for decreasing guide width and produce the net transmission enhancement seen in figure 9.

While a determination of coupling efficiency η to specific waveguide modes cannot be determined, it is possible to define the losses to quenching through the sum of waveguide coupling and coupling to free-space modes. With this determined the remaining light can be considered both plasmonically and photonically non-radiative, and is seen in figure 10(b). This system shows significant quenching losses up to 100 nm trench systems; however there is a distinct minimum in quenching losses for 60 nm trench systems. This is due to the greatly increased preferential coupling to waveguide modes at this geometry reducing power available to be lost to quenching.

The coupling fraction together with Purcell factor can be used to define a new FoM, which encompasses the mode area, propagation length and coupling fraction to remain dimensionless:

$$M = \sqrt{\frac{\pi}{A_{\text{eff}} \text{Im}(k_{\text{spp}})}} F_p \eta. \quad (2)$$

The new FoM weights the modes for each width based on the coupling efficiency of the enhanced total luminescence to that mode, i.e. the useful fraction of the enhanced emission; however the applicability of this quantity is reduced to cases in which the mode being coupled to can be accurately determined through power flow measurements. For the trenches observed it is however impossible to deconvolute components of each mode existing within the trench, particularly at the corners which exhibit the greatest power flow.

4. Summary and discussion

Numerical analysis of the SPP modes within trench waveguide systems provides detailed information on the mode field components, effective indices, propagation lengths and mode areas. The definition of various figures of merit has allowed determination of optimum waveguide geometries for propagation and coupling from emitters within the trench to SPP modes. From these results, and with considerations for practicality of fabrication, it is determined a trench of 50 nm width in 100 nm Au will provide balance with propagation and coupling, with fabrication a drive towards 20 nm trenches as ideal, with a single wall break to define an emission area of ideal width <100 nm suited for practical devices.

Such trench waveguide systems offer extremely high confinement with propagation on length scales appropriate to local interconnects (i.e. the μm scale), along with high efficiency coupling to SPP modes within the system, which can be close to 80% (seen in figure 10) as determined through numerical analysis. The large Purcell factor exhibited in these structures will further lead to faster modulation capabilities along with an increased quantum yield important for the realization of the proposed PED.

The confinement of these modes to widths on the order of 50 nm is approaching that of the expected necessary dimensions for interconnects by 2020, and the delay for these systems over the shorter $5\mu\text{m}$ length scales will be on the order of 0.1 ps for the slowest modes of the system, and significantly less for the faster modes; both of which are an order of magnitude lower than those reported by the International Technology Roadmap for Semiconductors (ITRS) [1].

Acknowledgements

This work was supported, in part, by EPSRC (UK) and Intel (Ireland/USA). AZ acknowledges support from the Royal Society and the Wolfson Foundation.

References

- [1] Arden W 2005 *International Technology Roadmap for Semiconductors: Interconnect* edn 2005
- [2] Conway J A, Sahni S and Szkopek T 2007 *Opt. Express* **15** 4474
- [3] Dai D and He S 2009 *Opt. Express* **17** 16646
- [4] Krasavin A V and Zayats A V 2011 *Opt. Lett.* **36** 3127
- [5] Holmgaard T, Chen Z, Bozhevolnyi S I, Markey L, Dereux A, Krasavin A V and Zayats A V 2009 *Appl. Phys. Lett.* **94** 051111
- [6] Krasavin A V and Zayats A V 2010 *Opt. Express* **18** 11791
- [7] Zia R, Selker M, Catrysse P and Brongersma M 2004 *J. Opt. Soc. Am. A* **21** 2442
- [8] Park J, Kim K, Lee I, Na H, Lee S and Lee B 2010 *Opt. Express* **18** 598
- [9] Neira A D, Wurtz G A, Ginzburg P and Zayats A V 2014 *Opt. Express* **22** 10987
- [10] Krasavin A V and Zayats A V 2012 *Phys. Rev. Lett.* **109** 053901
- [11] Shalin A S, Ginzburg P, Belov P A, Kivshar Y S and Zayats A V 2014 *Laser Photonics Rev.* **8** 131
- [12] Krasavin A V, Vo T P, Dickson W, Bolger P M and Zayats A V 2011 *Nano Lett.* **11** 2231
- [13] Krasavin A V, Randhawa S, Bouillard J, Renger J, Quidant R and Zayats A V 2011 *Opt. Express* **19** 25222
- [14] Kéna-Cohen S, Stavrinou P N, Bradley D D C and Maier S A 2013 *Nano Lett.* **13** 1323
- [15] Fedyanin D Y, Krasavin A V, Arsenin A V and Zayats A V 2012 *Nano Lett.* **12** 2459
- [16] Bolger P M, Dickson W, Krasavin A V, Liebscher L, Hickey S G, Skryabin D V and Zayats A V 2010 *Opt. Lett.* **35** 1197
- [17] Veronis G and Fan S 2005 *Opt. Lett.* **30** 3359
- [18] Huang K C Y, Seo M, Sarmiento T, Huo Y, Harris J S and Brongersma M L 2014 *Nat. Photonics* **8** 244
- [19] Kafafi Z 2005 *Organic Electroluminescence* (London: Taylor and Francis)
- [20] Krasavin A V and Zayats A V 2010 *Appl. Phys. Lett.* **97** 041107
- [21] Chiu N, Yu C, Nien S, Lee J, Kuan C, Wu K, Lee C and Lin C 2007 *Opt. Express* **15** 11608
- [22] Nowy S, Krummacher B C, Frischeisen J, Reinke N A and Bruetting W 2008 *J. Appl. Phys.* **104** 123109
- [23] Koller D M, Hohenau A, Dittbacher H, Galler N, Reil F, Aussenegg F R, Leitner A, List E J W and Krenn J R 2008 *Nat. Photonics* **2** 684

- [24] Al-Ibrahim M, Roth H K, Schroedner M, Konkin A, Zhokhavets U, Gobsch G, Scharff P and Sensfuss S 2005 *Org. Electron.* **6** 65
- [25] Park Y D, Kim D H, Jang Y, Cho J H, Hwang M, Lee H S, Lim J A and Cho K 2006 *Organ. Electron.* **7** 514
- [26] Palik E D 1984 *J. Opt. Soc. Am. A* **1** 1297
- [27] Zhokhavets U, Gobsch G, Hoppe H and Sariciftci N S 2004 *Thin Solid Films* **451** 69
- [28] Berini P and Buckley R 2007 *Opt. Express* **15** 12174
- [29] de Fornel P, Lourtioz J, Pagnoux D, Benisty H, Berger V, Gerard J, Maystre D and Tchelnokov A 2008 *Photonic Crystals: Towards Nanoscale Photonic Devices* (Berlin: Springer)
- [30] Barnes W L 1998 *J. Mod. Opt.* **45** 661
- [31] Purcell E M 1946 *Proc. Am. Phys. Soc.* **69** 681
- [32] Taflove A, Oskooi A and Johnson S G 2013 *Advances in FDTD Computational Electrodynamics* (Boston, MA: Artech House Publishers)